Active Nematic Defects and Epithelial Morphogenesis

Farzan Vafa[1,2] and L. Mahadevan[3,4]
[1]Department of Physics, University of California Santa Barbara, Santa Barbara, California 93106, USA
[2]Center of Mathematical Sciences and Applications, Harvard University, Cambridge, Massachusetts 02138, USA
[3]School of Engineering and Applied Sciences, Harvard University, Cambridge, Massachusetts 02138, USA
[4]Departments of Physics, and Organismic and Evolutionary Biology, Harvard University, Cambridge, Massachusetts 02138, USA

(Received 14 May 2021; revised 11 April 2022; accepted 25 May 2022; published 26 August 2022)

Inspired by recent experiments that highlight the role of nematic defects in the morphogenesis of epithelial tissues, we develop a minimal framework to study the dynamics of an active curved surface driven by its nematic texture. Allowing the surface to evolve via relaxational dynamics leads to a theory linking nematic defect dynamics, cellular division rates, and Gaussian curvature. Regions of large positive (negative) curvature and positive (negative) growth are colocalized with the presence of positive (negative) defects. In an ex-vivo setting of cultured murine neural progenitor cells, we show that our framework is consistent with the observed cell accumulation at positive defects and depletion at negative defects. In an in-vivo setting, we show that the defect configuration consisting of a bound $+1$ defect state, which is stabilized by activity, surrounded by two $-1/2$ defects can create a stationary ring configuration of tentacles, consistent with observations of a basal marine invertebrate *Hydra*.

DOI: 10.1103/PhysRevLett.129.098102

Morphogenesis, the development of a self-organized form in biology, results from the complex interplay of mechanical and biochemical processes [1–3]. To understand the dynamics of form, we need to complement our knowledge of the molecular constituents that unify many developmental programs with coarse-grained theories that couple flows, forces, and self-regulation to generate shape and link them to testable experimental predictions [4–7]. At the cellular level, there are four geometric fields—cell number, size, shape, and position—that vary in space and time and are responsible for generating shape. In plant tissues, where cells do not change their relative positions, there has been much progress in linking molecular and cellular processes to tissue shaping [8,9], while in animal tissues, the ability to tag and track thousands of cells in space and time [10–12] allow us to begin answering similar questions linking cellular processes to tissue shape [13–15].

A particularly intriguing question in thin layered epithelial tissues is the role of topological defects in controlling morphogenesis, seen in experimental observations of cell extrusion [16,17], layer formation [18], and body shaping using bulges, pits, and tentacles [19]. Complementing work on the role of defects in passive surfaces that allow the *induced* geometry to relax e.g., [20–22], here we address how topological defects couple to the intrinsic geometry of surfaces (Fig. 1) via a minimal theory for the relaxational dynamics of the *intrinsic* geometry of active epithelial surfaces (see Ref. [23] for a recent review). Our model of epithelial layers is a dynamical theory of active nematics, which consist of head-tail symmetric, elongated units that consume energy to move and do work on their surroundings, while still tending to align, locally generating nematic (apolar) order [24–26]. Like their passive counterparts, active nematics exhibit singular distortions, i.e., topological defects which interrupt the nematic order (see Supplemental Material (SM) [27], *Elementary topological defects and their bound states*, for a brief overview).

A minimal model that couples the relevant degrees of freedom in an active system must allow for spatiotemporal variations in the two-dimensional nematic tensor Q^{ab}, an

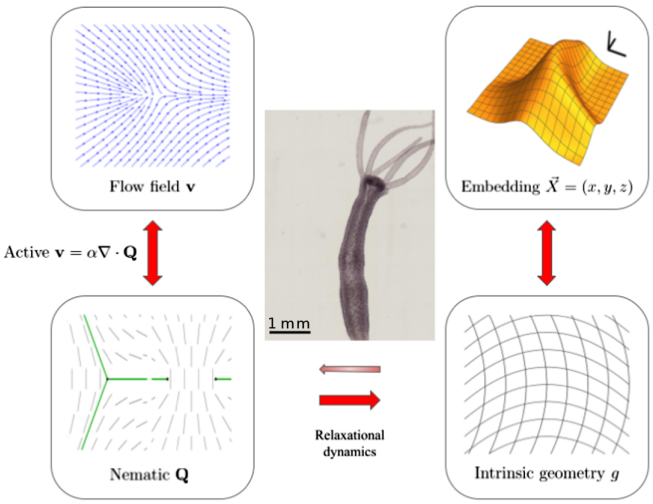

FIG. 1. Schematic of our model. Epithelial activity driven by a nematic texture leads to a flow field that drives nematic defects. The defects then induce variations in the intrinsic metric and thence changes in the 3D embedding of the epithelial surface. Image of *Hydra* in the center, adapted from [28].

active velocity field v^a determined by the local nematic field, and the geometry of the sheet, characterized by its 2D metric g_{ab} (which can be deduced from tissue geometry), and its embedding in three dimensions. For simplicity, we will assume that how the surface sits in 3D (the extrinsic geometry) can be deduced entirely by the shape of the 2D surface (the intrinsic geometry), and that the dynamics of the other fields follows a combination of variations in the free energy and active flow dynamics.

The two main contributions to the free energy that we consider are due to (i) the nematic tensor $Q^{ab} = A[\hat{n}^a\hat{n}^b - \frac{1}{2}\delta^{ab}]$, where A is the magnitude of the nematic order and $\hat{n}^\mu$ is the local director field (ii) the metric g_{ab}. Then the total free energy $\mathcal{F}$ is the sum of contributions from the nematic field as well as from the intrinsic metric, with $\mathcal{F} = \mathcal{F}_Q + \mathcal{F}_g$. Here, the two-dimensional Landau-de Gennes free energy [29], $\mathcal{F}_Q$, in its covariant form, is given by

$$\begin{aligned}\mathcal{F}_Q &= \int d^2x\sqrt{g}\Big[\tilde{K}g_{bd}\nabla_a Q^{ab}\nabla_c Q^{cd} - K'R\,\mathrm{Tr}[Q^2] \\ &\quad + \frac{1}{4}\epsilon^{-2}(1 - 2g_{bc}g_{ad}Q^{ab}Q^{cd})^2\Big] \\ &= \int d^2x\sqrt{g}\Big[\tilde{K}\,\mathrm{Tr}[(\nabla\cdot Q)^2] - K'R\,\mathrm{Tr}[Q^2] \\ &\quad + \frac{1}{4}\epsilon^{-2}(1 - 2\,\mathrm{Tr}[Q^2])^2\Big] \end{aligned} \tag{1}$$

where g_{ab} is the metric, ∇_a is the covariant derivative, and R is the scalar curvature. Here $\tilde{K}$ is the Frank elasticity parameter in the single-constant approximation, $K' > 0$ is a curvature elasticity that can be viewed as a geometric contribution to the potential: with $R > 0$ (< 0), this term favors a ordered (disordered) state, while the last term governs the isotropic-nematic transition, with ϵ controlling the microscopic nematic correlation length [30]. We further assume that the surface relaxes via relaxational dynamics analogous to diffusion; a naturally invariant form is then given by Ricci flow [31],

$$\partial_t g_{ab} = -DR_{ab} + \lambda g_{ab} \tag{2}$$

where R_{ab} is the Ricci tensor (which in 2D is given by $R_{ab} = \frac{1}{2}Rg_{ab}$), $D > 0$ is the diffusivity, and $\lambda(t) > 0$ controls the growth rate of the area. In general, $\lambda = \lambda(x,t)$, but for simplicity we will take $\lambda = \lambda(t)$. Equation (2) follows from the gradient flow of the free energy $\mathcal{F}_g = \int d^2x\sqrt{g}[K_\varphi R\varphi - \lambda]$ where $\sqrt{g} = \exp(\varphi)$ [32]. $K_\varphi(\propto D)$ is an elastic constant penalizing changes in the Gaussian curvature R.

Then the coupled dynamics of the nematic and metric fields associated with gradient descent and advection by a nonequilibrium flow v^c [33] yields

$$\partial_t Q^{ab} = -v^c\nabla_c Q^{ab} + [Q,\Omega]^{ab} - \gamma_Q^{-1}g^{ac}g^{bd}\frac{1}{\sqrt{g}}\frac{\delta\mathcal{F}}{\delta Q^{cd}}, \tag{3}$$

$$\partial_t g_{ab} = -(\nabla_a v^c)g_{cb} - (\nabla_b v^c)g_{ca} - \gamma_\varphi^{-1}\frac{1}{\sqrt{g}}\frac{\delta\mathcal{F}}{\delta g^{ab}}, \tag{4}$$

with $\Omega_{ab} = (\nabla_a v_b - \nabla_b v_a)/2$ the vorticity, and γ_Q and γ_φ are the viscous coefficients for the dynamics of Q^{ab} and g_{ab}, respectively, with units of radians^2/time.

Closure of the system (3)–(4) requires an equation for the active velocity field generated by the active stress σ^{ab}. We note that in Eq. (3) we have ignored the rate of strain alignment; in the biologically relevant, overdamped limit described by Eq. (5) this effect leads to a renormalization of the rigidity constant [34,35]. In this context, $\sigma^{ab} = \tilde{\alpha}Q^{ab}$ [24,36]; i.e., we balance the active stresses with the substrate friction (neglecting elastic and nonlocal hydrodynamic effects [37]), and therefore write [33]

$$\mu v^c = \tilde{\alpha}\nabla_a Q^{ac}. \tag{5}$$

Here μ is the substrate friction, $\tilde{\alpha}$ is the active energy density with $\tilde{\alpha} > 0$ ($\tilde{\alpha} < 0$) corresponding to contractile (extensile) activity. We define the scaled activity coefficient $\alpha = \tilde{\alpha}/\mu$.

In terms of the problem parameters, $\tilde{K}$, K', ϵ, α, K_φ, γ_Q, γ_φ, and the system size L, we can define the nematic coherence length (or defect core radius) $\xi = \sqrt{\tilde{K}}\epsilon$, the geometric coherence length $\ell_\varphi = \sqrt{K_\varphi}\epsilon$, a "Gaussian curvature" length $\ell_{R,Q} = \sqrt{K'}\epsilon$, and $\ell_d = \sqrt{K/|\tilde{\alpha}|}$, the defect separation length [38], and the relaxation times $\tau_Q = \gamma_Q\epsilon^2$ and $\tau_\varphi = \gamma_\varphi L^2/K_\varphi$. This leads to the following dimensionless quantities: ξ/ℓ_φ, the ratio of coherence lengths for the nematic field and intrinsic geometry (< 1 because extrinsic geometry variations occur on scales large compared to the nematic defect core size), $\tau_\varphi/\tau_Q = (\gamma_\varphi/\gamma_Q)(L/\ell_\varphi)^2$ ($\gg 1$ because we assume that the long wavelength extrinsic geometry relaxes slowly compared to the local nematic order), and $K/K' \sim 1$, where $K = \tilde{K} - K'$, which as we will discuss later is the ratio of the two different types of nematic elastic deformations. See SM [27], *Model Parameters*, for estimates of model parameters.

Equations (3)–(5) form a set of nonlinear partial differential equations that dictate the evolution of the nematic field Q^{ab} and the metric tensor g_{ab} as a function of the activity α, when complemented by appropriate initial and boundary conditions. To make progress in a minimal setting for epithelial morphogenesis, we choose 2D isothermal (conformal) [39] complex coordinates z and $\bar{z}$ such that

$$ds^2 = g_{z\bar{z}}dzd\bar{z} + g_{\bar{z}z}d\bar{z}dz = 2g_{z\bar{z}}|dz|^2 = e^\varphi|dz|^2 \tag{6}$$

and assume that the metric remains diagonal in these coordinates for all time. Furthermore, as the nematic tensor Q^{ab} is a traceless real bivector, we can write its components $Q = Q^{zz}$, $\bar{Q} = Q^{\bar{z}\bar{z}}$, and $Q^{z\bar{z}}$, with $Q^{z\bar{z}} = 0$, and $Q = (\bar{Q})^*$. Since the metric $g_{z\bar{z}}$ measures the area in the z coordinate

system, assuming fixed cell size, this implies that we can interpret $\varphi = \log g_{z\bar{z}}$, i.e., the log of the cell density in these coordinates so that, the change in φ reflects cell division.

In these coordinates, $\mathcal{F}_Q$ takes the form

$$\begin{aligned}\mathcal{F}_Q &= \int d^2z\sqrt{g}\Big[2Kg_{z\bar{z}}\nabla_z Q^{zz}\nabla_{\bar{z}}Q^{\bar{z}\bar{z}} + 2K' g_{z\bar{z}}\nabla_{\bar{z}}Q^{zz}\nabla_z Q^{\bar{z}\bar{z}} \\ &\quad + \frac{1}{4}\epsilon^{-2}(1-4g_{z\bar{z}}g_{z\bar{z}}Q^{zz}Q^{\bar{z}\bar{z}})^2\Big] \\ &= \int d^2z\sqrt{g}\Big[2K|\nabla_z Q|^2 + 2K'|\nabla_{\bar{z}}Q|^2 \\ &\quad + \frac{1}{4}\epsilon^{-2}(1-4|Q|^2)^2\Big] \end{aligned} \tag{7}$$

where $K = \tilde{K} - K' > 0$ to guarantee positivity of the elastic energy, $Q = Q^{zz}$ and $\bar{Q} = Q^{\bar{z}\bar{z}}$, and $|\cdot|$ is defined in terms of the metric [40]. Here the covariant derivatives $\nabla_z Q^{zz} = \partial Q + 2(\partial\varphi)Q$ and $\nabla_{\bar{z}}Q^{zz} = \bar{\partial}Q$, while the scalar curvature $R = -4e^{-\varphi}\partial\bar{\partial}\varphi$. The asymmetry in the appearance of $\partial\varphi$ in $\nabla_z Q$ and $\nabla_{\bar{z}}$ is the underlying reason behind asymmetry in cell growth near defects: cells accumulate at positive defects and deplete at negative defects.

As a preliminary step before considering active defects, we consider the case of passive nematics with $\alpha = 0$. Then the dynamics for Q and φ in isothermal conformal coordinates can be written as

$$\begin{aligned}\gamma_Q\partial_t Q &= 2Kg^{z\bar{z}}\nabla_{\bar{z}}\nabla_z Q + 2K' g^{z\bar{z}}\nabla_z\nabla_{\bar{z}}Q \\ &\quad + 2\epsilon^{-2}(1-4|Q|^2)Q, \end{aligned} \tag{8}$$

$$\begin{aligned}\gamma_\varphi\partial_t\varphi &= -K_\varphi R + 4K|\nabla_z Q|^2 + 4Kg_{z\bar{z}}(Q\nabla_z\nabla_{\bar{z}}\bar{Q} + \bar{Q}\nabla_{\bar{z}}\nabla_z Q) \\ &\quad - 4K'|\nabla_{\bar{z}}Q|^2 - \frac{1}{4}\epsilon^{-2}(1-4|Q|^2)(1-20|Q|^2) + \lambda, \end{aligned} \tag{9}$$

where the covariant derivative terms are $\nabla_{\bar{z}}\nabla_z Q = \bar{\partial}\partial Q + 2(\bar{\partial}\partial\varphi)Q + 2\partial\varphi\bar{\partial}Q$ and $\nabla_z\nabla_{\bar{z}}Q = \partial\bar{\partial}Q + 2\partial\varphi\bar{\partial}Q$.

For a flat configuration with $\varphi = 0$, denoting $\varphi^\pm$ and $Q^\pm$ as the local geometry and nematic field in the neighborhood of $\pm 1/2$ defects, Eq. (9) in the neighborhood of a defect simplifies to

$$\begin{aligned}\gamma_\varphi\partial_t\varphi^+ &= 4K|\partial Q^+|^2 + 2K(Q^+\partial\bar{\partial}\bar{Q}^+ + \bar{Q}^+\bar{\partial}\partial Q^+) \\ &\quad - 4K'|\bar{\partial}Q^+|^2 - \frac{1}{4}\epsilon^{-2}(1-4|Q^+|^2)(1-20|Q^+|^2) \\ &\quad + \lambda, \end{aligned} \tag{10}$$

$$\begin{aligned}\gamma_\varphi\partial_t\varphi^- &= 4K|\partial Q^-|^2 + 2K(Q^-\partial\bar{\partial}\bar{Q}^- + \bar{Q}^-\bar{\partial}\partial Q^-) \\ &\quad - 4K'|\bar{\partial}Q^-|^2 - \frac{1}{4}\epsilon^{-2}(1-4|Q^-|^2)(1-20|Q^-|^2) \\ &\quad + \lambda. \end{aligned} \tag{11}$$

Noting that $Q^+ = (Q^-)^*$ and that in the vicinity of the positive (negative) defect core, $\bar{\partial}Q^+$ $(\partial Q^-) = 0$ leads to

$$\begin{aligned}\gamma_\varphi\partial_t\varphi^+ - \gamma_\varphi\partial_t\varphi^- &= 4K|\partial Q^+|^2 + 4K'|\bar{\partial}Q^-|^2 \\ &= 4\tilde{K}|\partial Q^+|^2 > 0. \end{aligned} \tag{12}$$

Interpreting φ as the logarithm of the cell density (since the Gaussian curvature $R = -4e^{-\varphi}\partial\bar{\partial}\varphi$), in the absence of net surface growth, this implies that φ will increase at a $+1/2$ defect and decrease near a $-1/2$ defect (since the two changes must balance each other), and the cell density will increase (decrease) at plus (minus) defects, i.e., cells accumulate (deplete) at the defects. This shows that in a passive setting without activity, positive curvature growth via a positive defect can still occur. The mechanism we propose is a geometric alternative to previously proposed mechanisms for cell accumulation at topological defects due to anisotropic friction [17,18], and can operate either independently or together with previously proposed mechanisms.

In the top panel of Fig. 2, we show the initial profile of φ at $t = 0$ from our analysis, showing the dynamic asymmetry between a plus and minus defect, consistent with the experimental observations of cell density in the vicinity of defects in murine neural progenitor epithelia [17]. In the bottom panel of Fig. 2, we show that this asymmetry in the shape in the neighborhood of $\pm 1/2$ defects is reflected in the Gaussian curvature of the surface which is positive (negative) near a plus (minus) defect, consistent with independent observations in a different experiment [19].

Activity, i.e., $\alpha \neq 0$, leads to anisotropic flow because of gradients in the nematic order parameter; this acts as an additional source of geometric frustration, modifying the Gaussian curvature of the sheet dynamically (see [27], *Geometric diffusion and Ricci flow*). More generally, to account for advective flow, we rewrite the coupled Eqs. (8) and (9) in complex coordinates with $\partial_t Q \to D_t Q = \partial_t Q + v^z\nabla_z Q + v^{\bar{z}}\nabla_{\bar{z}}Q - (\nabla_z v^z - \nabla_{\bar{z}}v^{\bar{z}})Q$ and $\partial_t\varphi \to D_t\varphi = \partial_t\varphi + 2(\nabla_z v^z + \nabla_{\bar{z}}v^{\bar{z}})$, where in the overdamped limit, $v^z = \alpha\nabla_z Q = \alpha[\partial Q + 2(\partial\varphi)Q]$ and $\nabla_z v^z = \partial_z v^z + (\partial\varphi)v^z$. To solve these equations and follow the nematic field and the intrinsic geometry, we use a finite-difference scheme with periodic boundary conditions to simulate a ringlike structure seen in *Hydra* (see SM [27], *Numerical Methods*).

We find that an initially flat geometry with a single $+1$ defect in the center and two $-1/2$ defects on the edges, using the ansatz from [41], settles into a stationary defect configuration of a ring of equally spaced $+1$ defects (bound state of two $+1/2$ defects) separated by pairs of $-1/2$ defects in a cylindrical geometry [see Fig. 3(a)], similar to that observed in [19]. Activity plays a key role in stabilizing this configuration, and in particular, the $+1$ bound state is a result of balance between Coulombic repulsion of the defects and active motility (see SM [27], *Elementary topological defects and their bound states*). Indeed, the larger the activity parameter for the extensile case $\alpha < 0$,

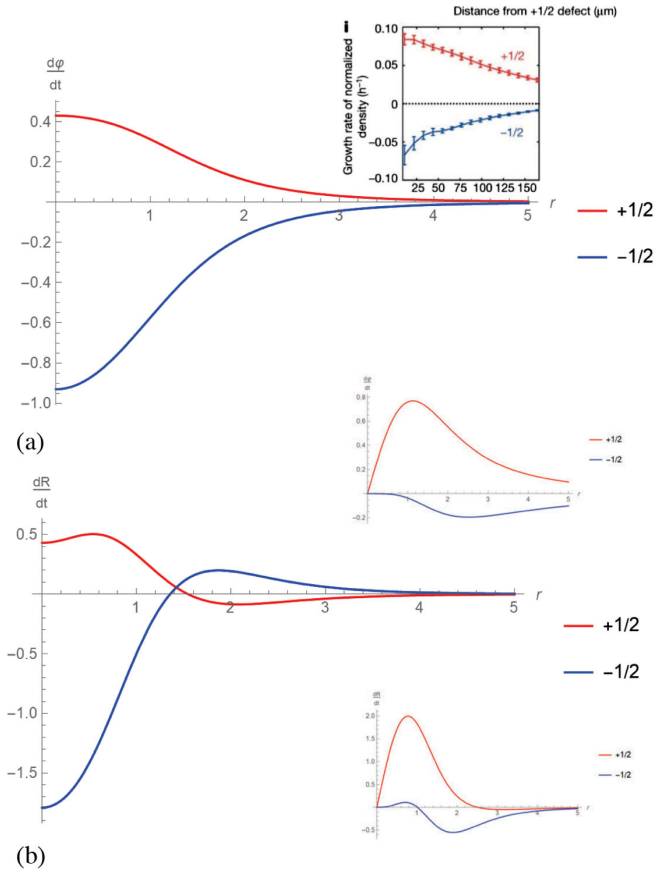

FIG. 2. Dynamics near defects. Following Eqs. (10) and (11), where $R = -4e^{-\varphi}\partial\bar{\partial}\varphi$, we show plots of (a) $(d\varphi/dt)$ and (b) (dR/dt) for a single $+1/2$ (in red) and a single $-1/2$ defect (in blue), with the activity $\alpha = 0$. Top inset: for comparison, we show the experimental growth rate of normalized cell density [17]. Middle and bottom insets: corresponding plots of active contribution for $(d\varphi/dt)$ and (dR/dt) for $\phi = 0$, $\alpha = 1$. Parameters used are $K = 1$, $K' = 1$, and $\epsilon = 1$.

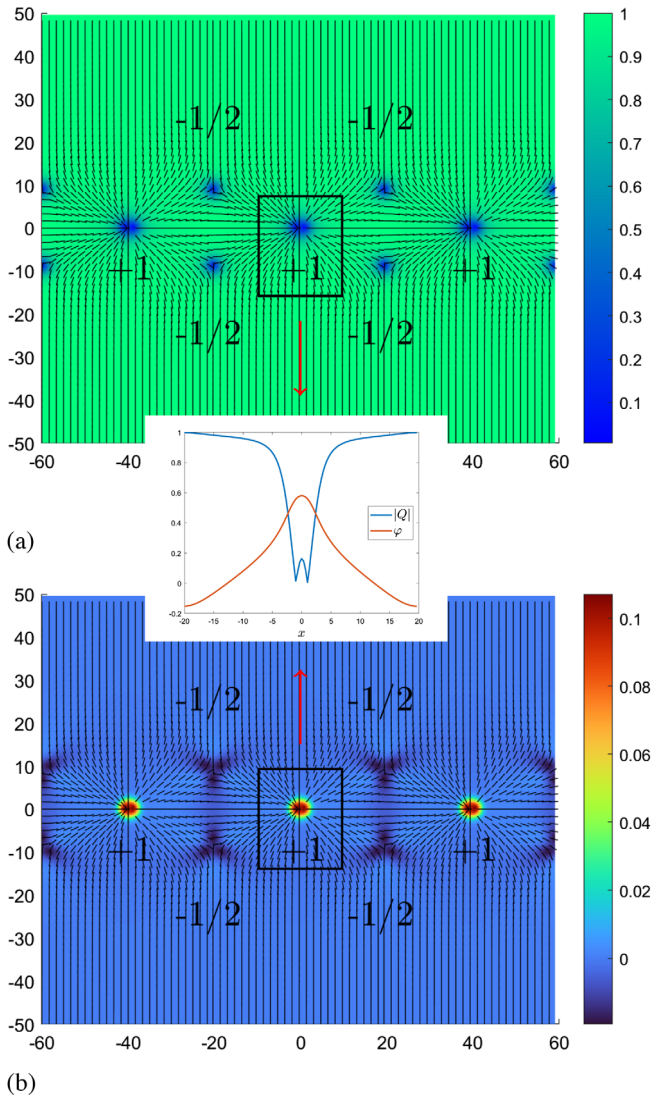

FIG. 3. Defect texture and geometry. We numerically integrate Eqs. (8) and (9) (with the substitution $\partial_t \to D_t$) to obtain steady state plots of (a) the magnitude of the nematic order parameter $|Q|$ and (b) the curvature density (given by $-4\partial\bar{\partial}\varphi$). We note that the sign of the curvature correlates with the sign of the defect, and that the defect configuration is a lattice of $+1$ bound states separated by pairs of $-1/2$ defects. In the inset, we show the profile of the nematic order $|Q|$ (blue) and φ (red) along the x axis. The profile of $|Q|$, which is dictated by the nematic coherence length, is smaller than the width of the profile of φ since $\ell_\varphi > \xi$. Parameters for simulations: $\alpha = -0.8$, $K = 1$, $K' = 0$, $\gamma_Q = \gamma_\varphi = 1$, $K_\varphi = 4$, and $\epsilon = 2$, in terms of which $\xi = 1$, $\ell_{R,Q} = 1$, and $\ell_\varphi = 2$. See text and SM [27], *Numerical methods*, for details.

the tighter is the $+1$ bound defect. Moreover, the curvature is positive near a plus defect, and negative near a minus defect, as can be seen in Fig. 3(b). Plotting the profiles of $|Q|$ and φ along the vertical x axis, we find that the peak in φ near the origin indicates outward bulging of the geometry. Additionally, the profile of $|Q|$ which is dictated by the nematic coherence length is much narrower than the width of φ, consistent with the expectation that the geometric coherence length is larger than the nematic coherence length, i.e., $\ell_\varphi > \xi$, similar to experimental observations [17] and numerical simulations [42]. (See SM [27], *Additional plots*, for a plot of the flow field at a late time.)

To ground these results, we turn to observations of epithelial morphogenesis in *Hydra*, a small, fresh-water basal marine invertebrate that has been a model organism for studying the dynamics of body shaping [19,43,44]. The tubular body of the organism consists of a bilayer of epithelial cells which contains condensed supracellular actin fibers which align parallel to the body axis in the outer (ectoderm) layer and perpendicular to the body axis in the inner (endoderm) layer [45]. A variable number of tentacles form a ring around the body, near the head, and form when a single $+1$ defect is surrounded by a pair of $-1/2$ defects [19], with the sign of the curvature correlated with the sign of the defect, consistent with our results

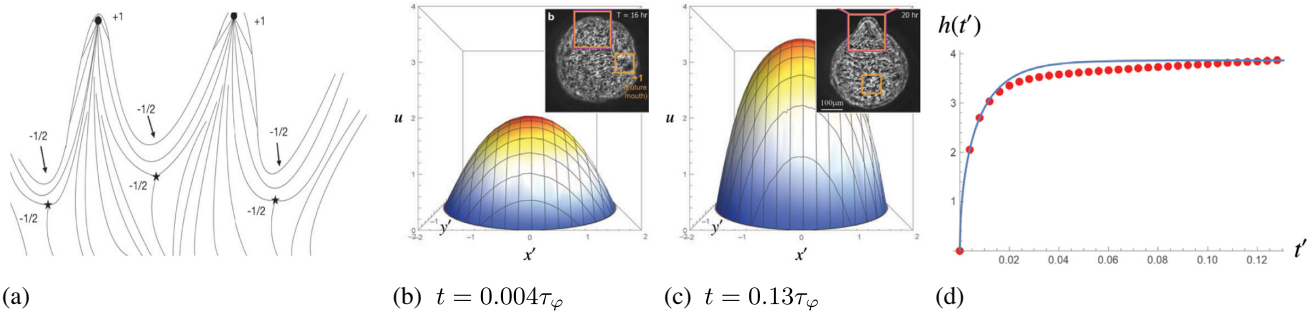

(a) (b) $t = 0.004\tau_\varphi$ (c) $t = 0.13\tau_\varphi$ (d)

FIG. 4. Extrinsic geometry. (a) Sketch of the geometry for the tentacle configuration from our simulation. The black dots represent $+1$ defects, the stars represent $-1/2$ defects, and black lines depict the nematic order. Three of the $-1/2$ defects are on the opposite side. (b), (c) Snapshots from simulations of height u of tentacle in real space near a $+1$ defect for early and late times, where insets (adapted from [19]) are snapshots of tentacle formation near a $+1$ defect for early and late times. (d) Plot of the height $h(t)$ at the center of the $+1$ defect as a function of time t. Red points are data from simulation and blue curve is the fit $h(t) = h_0[1 - \exp(-t/\tau)]^{1/2}$, where we find that $h_0 = 3.87L$ and $\tau = 0.01\tau_\varphi$. Initially, $h(t) \propto (L/\xi)(L/\ell_\varphi)L\sqrt{(t/\tau_\varphi)}$ and $\tau \propto \tau_\varphi$. See SM [27], *Algorithm for finding embedding*, for details. All plots use rescaled coordinates $x' = x/L$, $y' = y/L$, and $t' = t/\tau_\varphi$.

summarized in Fig. 3. Indeed, a qualitative rendering of the shape associated with the presence of these bound defect states shown in Fig. 4(a) provides a simple projective view of the body plan in the neighborhood of the ring of tentacles.

Although knowing the intrinsic geometry does not always allow us to deduce the extrinsic geometry completely, it is possible to get a numerical approximation (see SM [27], *Algorithm for finding embedding*) of the local shape of the active surface as shown in Figs. 4(b) and 4(c) near a $+1$ defect. This allows us to see that at early times the time evolution of the height follows the scaling law $h \propto \sqrt{t}$, which can be analytically derived by using Eq. (10) (see SM [27], *Dynamics of bud growth*).

Our minimal framework coupling the dynamics of an active nematic field on a curved surface to the intrinsic geometry of the surface via relaxational dynamics has focused on the interplay between geometry and nematic defects and leads to three simple conclusions: (i) the sign of the curvature is correlated with the sign of the defect, (ii) cells accumulate and form mounds at positive defects and are depleted at negative defects, and (iii) a stationary ring configuration of equally spaced $+1$ defects separated by pairs of $-1/2$ defects can form. These results are consistent with experimental observations in different systems such as neural progenitor cells in-vitro and *Hydra* morphogenesis in-vivo. Moving forward, a more complete description must include a complete characterization of the dynamics of embedding and the possible time dependence of isothermal coordinates, e.g., using phase field models for active deformable shells [42,46] that account for both the induced and the intrinsic geometry of the manifolds, but now including feedback on activity of the form $\alpha = \alpha(Q^{ab}, g_{ab}, \ldots)$, are potential directions for future work. Indeed, a recent paper [47] submitted contemparaneously has begun to address some closely related questions.

We thank Xianfeng David Gu and Shing-Tung Yau for valuable discussions on reconstructing the embedding from the intrinsic metric, and discussions with Suraj Shankar, and the Cristina Marchetti and Mark Bowick groups at UCSB. This work is partially supported by the Center for Mathematical Sciences and Applications at Harvard University (F. V.) and the NSF Simons Center for Mathematical and Statistical Analysis of Biology Award No. 1764269, the Simons Foundation (L. M.) and the Henri Seydoux Fund (L. M.).

[1] D. W. Thompson, *On Growth and Form* (Cambridge University Press, Cambridge, England, 1917).
[2] M. J. F. Barresi and S. F. Gilbert, *Developmental Biology*, 12th ed. (Sinauer Associates, New York, 2020).
[3] T. Lecuit and L. Mahadevan, Development **144**, 4197 (2017).
[4] C.-P. Heisenberg and Y. Bellaïche, Cell **153**, 948 (2013).
[5] P. Gross, K. V. Kumar, and S. W. Grill, Annu. Rev. Biophys. **46**, 337 (2017).
[6] L. Mahadevan, in *Proceedings of the 27th Solvay Conference on Physics: Physics of Living Matter*, edited by D. Gross and B. Shraiman (World Scientific, Singapore, 2020).
[7] C. Collinet and T. Lecuit, Nat. Rev. Mol. Cell Biol. **22**, 245 (2021).
[8] E. M. Meyerowitz, Cell **88**, 299 (1997).
[9] E. Coen, R. Kennaway, and C. Whitewoods, Development **144**, 4203 (2017).
[10] F. Bosveld, I. Bonnet, B. Guirao, S. Tlili, Z. Wang, A. Petitalot, R. Marchand, P.-L. Bardet, P. Marcq, F. Graner, and Y. Bellaïche, Science **336**, 724 (2012).
[11] R. Tomer, K. Khairy, F. Amat, and P. J. Keller, Nat. Methods **9**, 755 (2012).

[12] U. Krzic, S. Gunther, T. E. Saunders, S. J. Streichan, and L. Hufnagel, Nat. Methods **9**, 730 (2012).
[13] R. Farhadifar, J.-C. Röper, B. Aigouy, S. Eaton, and F. Jülicher, Curr. Biol. **17**, 2095 (2007).
[14] N. C. Heer and A. C. Martin, Development **144**, 4249 (2017).
[15] K. D. Irvine and B. I. Shraiman, Development **144**, 4238 (2017).
[16] T. B. Saw, A. Doostmohammadi, V. Nier, L. Kocgozlu, S. Thampi, Y. Toyama, P. Marcq, C. T. Lim, J. M. Yeomans, and B. Ladoux, Nature (London) **544**, 212 (2017).
[17] K. Kawaguchi, R. Kageyama, and M. Sano, Nature (London) **545**, 327 (2017).
[18] K. Copenhagen, R. Alert, N. S. Wingreen, and J. W. Shaevitz, Nat. Phys. **17**, 211 (2021).
[19] Y. Maroudas-Sacks, L. Garion, L. Shani-Zerbib, A. Livshits, E. Braun, and K. Keren, Nat. Phys. **17**, 251 (2021).
[20] T. C. Lubensky and J. Prost, J. Phys. II (France) **2**, 371 (1992).
[21] H. S. Seung and D. R. Nelson, Phys. Rev. A **38**, 1005 (1988).
[22] J. R. Frank and M. Kardar, Phys. Rev. E **77**, 041705 (2008).
[23] S. C. Al-Izzi and R. G. Morris, Semin. Cell Dev. Biol. **120**, 44 (2021).
[24] M. C. Marchetti, J.-F. Joanny, S. Ramaswamy, T. B. Liverpool, J. Prost, M. Rao, and R. A. Simha, Rev. Mod. Phys. **85**, 1143 (2013).
[25] A. Doostmohammadi, J. Ignés-Mullol, J. M. Yeomans, and F. Sagués, Nat. Commun. **9**, 3246 (2018).
[26] S. Shankar, A. Souslov, M. J. Bowick, M. C. Marchetti, and V. Vitelli, Nat. Rev. Phys. **4**, 380 (2022).
[27] See Supplemental Material at http://link.aps.org/supplemental/10.1103/PhysRevLett.129.098102, which additionally includes Refs. [48–60], for further details on topological defects, Ricci flow, model parameters, role of activity, numerical simulations, and dynamics of bud growth.
[28] D. J. Drew, Hydra (YPM IZ 091796), *Digital Image: Yale Peabody Museum of Natural History* (2018).
[29] P. G. de Gennes and J. Prost, *The Physics of Liquid Crystals* (Clarendon Press, Oxford, 1993).
[30] Unlike in situations where the metric remains fixed, as in the elastomeric case [61], here we allow it to vary dynamically, so that the liquid crystalline flows can generate curvature via defects. Moreover, in Ref. [61], positive defects generate negative curvature, contrary to both recent experiments [17,19] and our model and simulations.
[31] R. S. Hamilton, J. Diff. Geom. **17**, 255 (1982).
[32] This is a manifestation of the well-known trace anomaly, where the response of the system to conformal rescaling of the metric is proportional to the curvature R [62].
[33] A. N. Beris and B. J. Edwards, *Thermodynamics of Flowing Systems: With Internal Microstructure* (Oxford University Press, New York, 1994).
[34] P. Srivastava, P. Mishra, and M. C. Marchetti, Soft Matter **12**, 8214 (2016).
[35] E. Putzig, G. S. Redner, A. Baskaran, and A. Baskaran, Soft Matter **12**, 3854 (2016).
[36] R. A. Simha and S. Ramaswamy, Phys. Rev. Lett. **89**, 058101 (2002).
[37] In the limit that $K/(\alpha\mu L^2), \gamma/(\mu L^2) \ll 1$, where γ is the viscosity coefficient, we can neglect the elastic stress $\sigma^{ab}_{el} \sim [Q, (\delta\mathcal{F}/\delta Q)]^{ab}$ and viscous stress $\sigma^{ab}_{\rm vis} \sim \gamma(\nabla^a v^b + \nabla^b v^a)$, so that the active stresses are balanced by the local substrate friction.
[38] E. J. Hemingway, P. Mishra, M. C. Marchetti, and S. M. Fielding, Soft Matter **12**, 7943 (2016).
[39] F. David, in *Statistical Mechanics of Membranes and Surfaces*, 2nd ed., edited by D. Nelson, T. Piran, and S. Weinberg (World Scientific, Singapore, 2004), Chap. 7, pp. 149–209.
[40] In deriving this equation, we used the fact that up to a total derivative, $R\,\mathrm{Tr}[Q^2] = 2(|\nabla_z Q|^2 - |\nabla_{\bar{z}} Q|^2)$.
[41] F. Vafa, M. J. Bowick, M. C. Marchetti, and B. I. Shraiman, arXiv:2007.02947.
[42] L. Metselaar, J. M. Yeomans, and A. Doostmohammadi, Phys. Rev. Lett. **123**, 208001 (2019).
[43] B. Galliot, Int. J. Dev. Biol. **56**, 411 (2012).
[44] E. Braun and K. Keren, BioEssays **40**, 1700204 (2018).
[45] R. Aufschnaiter, R. Wedlich-Söldner, X. Zhang, and B. Hobmayer, Biol. Open **6**, 1137 (2017).
[46] A. Mietke, F. Jülicher, and I. F. Sbalzarini, Proc. Natl. Acad. Sci. U.S.A. **116**, 29 (2019).
[47] L. A. Hoffmann, L. N. Carenza, J. Eckert, and L. Giomi, Sci. Adv. **8**, eabk2712 (2022).
[48] V. Narayan, S. Ramaswamy, and N. Menon, Science **317**, 105 (2007).
[49] T. Sanchez, D. T. Chen, S. J. DeCamp, M. Heymann, and Z. Dogic, Nature (London) **491**, 431 (2012).
[50] L. Giomi, M. J. Bowick, X. Ma, and M. C. Marchetti, Phys. Rev. Lett. **110**, 228101 (2013).
[51] L. Pismen, Phys. Rev. E **88**, 050502(R) (2013).
[52] S. Shankar, S. Ramaswamy, M. C. Marchetti, and M. J. Bowick, Phys. Rev. Lett. **121**, 108002 (2018).
[53] K. Thijssen and A. Doostmohammadi, Phys. Rev. Research **2**, 042008(R) (2020).
[54] F. Vafa, arXiv:2009.10723.
[55] C. F. Gauss, in *A Source Book in Mathematics*, edited by D. E. Smith (Dover, New York, 1959), pp. 463–475.
[56] G. Perelman, arXiv:math/0211159.
[57] N. Kumar, R. Zhang, J. J. de Pablo, and M. L. Gardel, Sci. Adv. **4**, eaat7779 (2018).
[58] J.-D. Benamou, B. D. Froese, and A. M. Oberman, ESAIM**44**, 737 (2010).
[59] X. Gu, F. Luo, J. Sun, and S. T. Yau, Variational principles for Minkowski type problems, discrete optimal transport, and discrete Monge-Ampere equations, arXiv:1302.5472.
[60] L. Cui, X. Qi, C. Wen, N. Lei, X. Li, M. Zhang, and X. Gu, Comput.-Aided Des. Appl. **115**, 181 (2019).
[61] D. Duffy and J. S. Biggins, Soft Matter **16**, 10935 (2020).
[62] A. Polyakov, Phys. Lett. **103B**, 207 (1981).